IEEE Access
Multidisciplinary | Rapid Review | Open Access Journal

Received November 7, 2021, accepted November 29, 2021, date of publication December 27, 2021,
date of current version January 4, 2022.

Digital Object Identifier 10.1109/ACCESS.2021.3138764

Analysis and Implementation of Self-Packaged Multi-Layer Suspended Coplanar Waveguide and Its Applications in Filtering Circuits

JIAN-KANG XIAO, (Member, IEEE), JIAO ZHANG, AND JUN PU
School of Electro-Mechanical Engineering, Xidian University, Xi'an 710071, China

Corresponding author: Jian-Kang Xiao (jkxiao@xidian.edu.cn)

This work was supported in part by the National Natural Science Foundation of China under Grant 61871458.

ABSTRACT In this paper, ideal suspended coplanar waveguide model is analyzed by using conformal mapping method, and the characteristic impedance is formulated and verified. A self-packaged suspended coplanar waveguide (SCPW) using multi-layer PCB technique is proposed and implemented with a experimental insertion loss of no more than 0.5dB, and return loss of better than 15.8dB from DC to 10GHz, which eliminates the drawbacks of the traditional suspended circuits such as bulky size, heavy weight and difficult to be integration because of their indispensable metal cavity and mechanical assemble. Both self-packaging and inside/outside end connection are used to reduce the wave leakage. Based on the self-packaged multi-layer suspended coplanar waveguide, a high frequency selective and high isolated multi-resonator coupled diplexer with measured isolation of no less than 42.5dB, and out-of-band suppression of more than 37dB as well as multiple transmission zeros have been implemented. A reflectionless bandstop filter with a measured S_{11} attenuation of more than 13.8dB is also implemented for demonstrating the availability of the self-packaged multi-layer SCPW.

INDEX TERMS Suspended coplanar waveguide, self-packaging, transition, diplexer, reflectionless bandstop filter.

I. INTRODUCTION

Suspended microstrip/stripline circuits have been demonstrated of an improved quality factor [1]–[5] because of the reduced loss and dispersion. The traditional suspended microstrip/stripline has been used to implement microwave filters [1], [2], resonator [3], and oscillators [4], et al, however, the further applications of this kind of circuits have many difficulties because of the obvious drawbacks of large circuit size and heavy weight, which is dominantly due to the metal cavity. In communication systems, multi-layer circuits [6]–[8] have been paid more and more attention because of the vertical integration capabilities even for system-on-package. Recently, multi-layer substrate integrated suspended line (SISL) circuit [7] has been realized by using common PCB technique to overcome the disadvantages of the traditional suspended line circuits.

The associate editor coordinating the review of this manuscript and approving it for publication was Wenjie Feng.

Transmission lines are the basis of RF circuits. Full-wave analysis and quasi-static analysis [9] are usually be used for theoretical research on transmission lines, and as full-wave analysis requires a lot of numerical calculation, so quasi-static analysis which only needs solving two-dimensional potential field has become the preferred method for analyzing transmission lines, and analytical formulas also can be achieved

The first analytical formula for calculating CPW quasi-static parameters using conformal mapping method is performed by Wen [10], and later, Veyres and Hanna [11] extended the application of this method to CPW with limited size and dielectric thickness, and the feasibility had been demonstrated [12], [13]. However, these formulas only suitable to the case of transmission lines with a single dielectric substrate In practice, there are many cases of multilayer substrates, such as the cable in the integrated circuit which is either on the substrate or buried between two substrates In 1997, Chen and Chou [14] deduced analytical formulas for CPW on multilayer substrates by conformal mapping, and the results have been verified. In transmission line analysis,

the validity of conformal mapping completely depends on the assumption that the transmission mode is quasi-static. The quasi-static approximation is valid at frequencies below 100GHz [15].

In this paper, an ideal suspended coplanar waveguide model is analyzed by using conformal mapping, and a suspended coplanar waveguide with self-packaging and inside/outside end connection in air cavities has been proposed by using multi-layer PCB technique. In order to validate the applications of the proposed SCPW, a diplexer with multiple transmission zeros and high isolation using self-packaged SCPW is proposed, while a reflectionless bandstop filter is also designed. All of the proposed SCPW circuits have been fabricated and have been validated by experiment. The proposed SCPW circuits have both advantages of the coplanar waveguide and the cavity circuit, which include easy shunt and series with the other passive/active components, low weight, ordinary processing and manufacturing technique, easy integration with other components, and favorable electromagnetic compatibility not only because the ground and conductor strip are coplanar, but also because the self-packaging and outer end connection Meanwhile, the PCB cut air cavities bring reduced dielectric loss, which in return introduces enhanced quality factor, and the most important is that other components including circuit chips and power supplies can be put down easily in the reserved air cavities.

II. ANALYSIS OF SUSPENDED COPLANAR WAVEGUIDE BY USING CONFORMAL MAPPING METHOD

A. CONFORMAL MAPPING PROCESS OF THE IDEAL SUSPENDED COPLANAR WAVEGUIDE

An ideal suspended coplanar waveguide model with three zones labeled as I, II and III, respectively, has been proposed as shown in Fig. 1. The characteristic impedance of the circuit model can be achieved by the conformal mapping method.

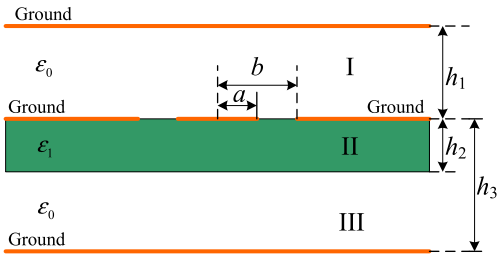

FIGURE 1. Ideal suspended coplanar waveguide structure.

For zone I, the capacitance per unit length is set to be C_1, and the conformal mapping process is plotted in Fig 2. Zone I is the inner region of a polygon on the zplane, as shown in Fig. 2(a) Firstly, the exponential transformation as

$$t = \exp(\frac{\pi z}{h_1}) \tag{1}$$

is used for transforming the rectangular area shown in Fig.2(a) into the lower part of the t-plane, as shown in

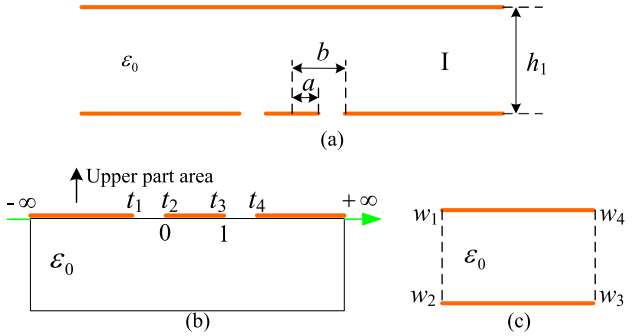

FIGURE 2. Schematic diagram of the transformation steps for solving C1. (a) z-plane. (b) t-plane. (c) w-plane.

Fig 2(b). Each point on the t-plane is corresponding to each point on the z-plane, that is $t_1 = \exp(-\pi b/h_1)t_2 = \exp(-\pi a/h_1)$, $t_3 = \exp(\pi a/h_1)$, $t_4 = \exp(\pi b/h_1)$ Then by using the Schwarz-Christoffel transformation, the lower part of the t-plane can be transformed into the rectangular domain of the w-plane, as shown in Fig. 2(c). The transformation from tplane to wplane is shown in Table 1.

TABLE 1. Transformation from t-plane to w-plane.

v	w_v	α_v	t_v	$(t-t_v)^{-\alpha_v/\pi}$
1	w_1	$\pi/2$	t_1	$(t-t_1)^{-1/2}$
2	w_2	$\pi/2$	t_2	$(t-t_2)^{-1/2}$
3	w_3	$\pi/2$	t_3	$(t-t_3)^{-1/2}$
4	w_4	$\pi/2$	t_4	$(t-t_4)^{-1/2}$

The integral transformation can be obtained by substituting into the Schwarz-Christoffel formula as

$$w = A_1 \int_{t_1}^{t} \frac{dt}{\sqrt{(t-t_1)(t-t_2)(t-t_3)(t-t_4)}} + B_1 \tag{2}$$

Here $w|_{t=0} = 0$, so $B_1 = 0$ The Antiderivative of the integral above can not be expressed as an elementary function [16]. If we set $r_1 = \frac{(t_3-t_1)(t-t_2)}{(t_3-t_2)(t-t_1)}$ [16], formula (2) can also be expressed as

$$w = A_1 \int_{t1}^{t} \frac{\frac{(t_3-t_1)(t_2-t_1)dt}{(t_3-t_2)(t-t_1)^2}(t-t_1)^2 \frac{(t_3-t_2)}{(t_3-t_1)(t_2-t_1)}}{\sqrt{(t-t_1)(t-t_2)(t-t_3)(t-t_4)}} \tag{3}$$

Then we can get the expression of $\overline{w_2w_3}$ as

$$\overline{w_2w_3} = A_1 g_1 k_1 \int_0^1 \frac{d\xi}{\sqrt{(1-\xi^2)(1-k_1^2\xi^2)}} = A_1 g_1 k_1 K(k_1) \tag{4}$$

with

$$k_1^2 = \frac{(t_3-t_2)(t_4-t_1)}{(t_4-t_2)(t_3-t_1)} \tag{5a}$$

$$\xi^2 = r_1 \tag{5b}$$

$$g_1 = \frac{2}{\sqrt{(t_3-t_2)(t_4-t_1)}} \tag{5c}$$

In the same way, $\overline{w_1w_2}$ can be obtained as

$$\overline{w_1w_2} = -jA_1g_1k_1K(k_1') \tag{6}$$

with

$$k_1' = \sqrt{1-k_1^2} \tag{7}$$

According to the well known parallel plate capacitor formula of $C = \varepsilon S/d$ the capacitance per unit length of zone I can be obtained as

$$C_1 = \varepsilon_0\frac{|\overline{w_2w_3}|}{|\overline{w_1w_2}|} = \varepsilon_0\frac{K(k_1)}{K(k_1')} \tag{8}$$

where $|\overline{w_2w_3}|$ represents the plate area of the parallel plate capacitor, $|\overline{w_1w_2}|$ is the parallel plate spacing, and ε_0 is the dielectric constant of air. $K(k_i)$ and $K(k_i$') are the first class of complete and incomplete elliptic integrals, respectively

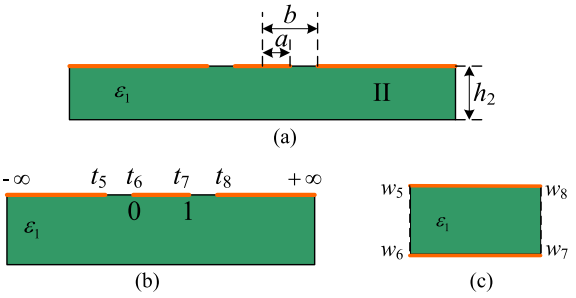

FIGURE 3. Schematic diagram of the transformation steps for solving C_2. (a) z-plane. (b) t-plane. (c) w-plane.

For zone II, the solution process of conformal mapping is shown in Fig 3. Firstly, the hyperbolic sine function

$$t = \sinh(\frac{\pi z}{2h_2}) \tag{9}$$

is used to transform the rectangular area with a width of h_2 on the z-plane as shown in Fig 3(a) into the lower part of the t-plane as shown in Fig3(b) through conformal mapping method. Where

$$t_5 = \sinh(-\frac{\pi b}{2h_2}), \quad t_6 = \sinh(-\frac{\pi a}{2h_2}) \tag{10a}$$

$$t_7 = \sinh(\frac{\pi a}{2h_2}), \quad t_8 = \sinh(\frac{\pi b}{2h_2}) \tag{10b}$$

Then Schwarz-Christoffel transformation is used to transform the lower part of the tplane into a rectangular domain of the wplane, as shown in Fig3(c). The transformation process is similar to that of zone I, and we have

$$\overline{w_6w_7} = A_2g_2k_2K(k_2) \tag{11}$$

$$\overline{w_5w_6} = -jA_2g_2k_2K(k_2') \tag{12}$$

The capacitance per unit length in zone II can be achieved as:

$$C_2 = \varepsilon_0(\varepsilon_1-\varepsilon_0)\frac{|\overline{w_6w_7}|}{|\overline{w_5w_6}|} = \varepsilon_0(\varepsilon_1-\varepsilon_0)\frac{K(k_2)}{K(k_2')} \tag{13}$$

where, ε_1 is the dielectric constant in zone II, and

$$k_2^2 = \frac{(t_7-t_6)(t_8-t_5)}{(t_8-t_6)(t_7-t_5)} \tag{14}$$

$$k_2' = \sqrt{1-k_2^2} \tag{15}$$

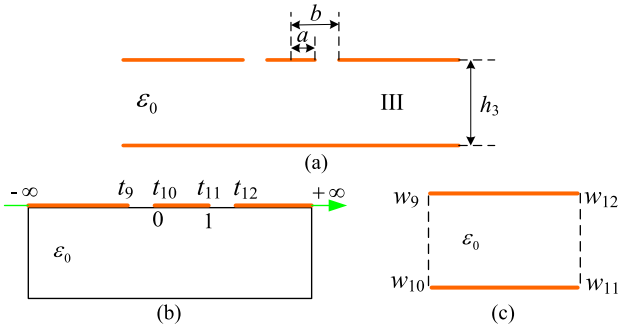

FIGURE 4. Schematic diagram of the transformation steps for solving C_3. (a) z-plane. (b) t-plane. (c) w-plane.

For zone III, the conformal mapping process is shown in Fig. 4, and which are similar to that of zone I Similarly, the exponential transformation as $t = \exp(\pi z/h_3)$ is used for transforming the z-plane shown in Fig.4(a) into t-plane, and we have $t_9 = \exp(-\pi b/h_3)$, $t_{10} = \exp(-\pi a/h_3)$, $t_{11} = \exp(\pi a/h_3)$, $t_{12} = \exp(\pi b/h_3)$ Then the t-plane as shown in Fig.4(b) is transformed into the w-plane, as shown in Fig. 4(c), and we get

$$\overline{w_{10}w_{11}} = A_3g_3k_3K(k_3) \tag{16}$$

$$\overline{w_9w_{10}} = -jA_3g_3k_3K(k_3') \tag{17}$$

The capacitance per unit length of zone III can be obtained as

$$C_3 = \varepsilon_0\frac{|\overline{w_{10}w_{11}}|}{|\overline{w_9w_{10}}|} = \varepsilon_0\frac{K(k_3)}{K(k_3')} \tag{18}$$

with

$$k_3^2 = \frac{(t_{11}-t_{10})(t_{12}-t_9)}{(t_{12}-t_{10})(t_{11}-t_9)} \tag{19a}$$

$$k_3{}' = \sqrt{1-k_3^2} \tag{19b}$$

B. BCHARACTERISTIC IMPEDANCE CALCULATION AND SIMULATION COMPARISON

The total capacitance per unit length of the suspended coplanar waveguide can be achieved as

$$\begin{aligned} C &= C_1 + C_2 + C_3 \\ &= \varepsilon_0\frac{K(k_1)}{K(k_1')} + \varepsilon_0(\varepsilon_1-\varepsilon_0)\frac{K(k_2)}{K(k_2')} + \varepsilon_0\frac{K(k_3)}{K(k_3')} \end{aligned} \tag{20}$$

while the effective dielectric constant ε_{eff} and fill factor q_i can be expressed respectively as

$$\varepsilon_{\text{eff}} = \frac{C'}{C''} = q_1\varepsilon_0 + q_2\varepsilon_0(\varepsilon_1-\varepsilon_0) + q_3\varepsilon_0 \tag{21}$$

$$\mathrm{q}_i = \frac{\frac{K(k_i)}{K(k_i')}}{\frac{K(k_1)}{K(k_1')} + \frac{K(k_3)}{K(k_3')}} \quad (i = 1, 2, 3) \tag{22}$$

Here, C' represents the capacitance per unit length filled with mixed media, and C'' represents the capacitance per unit length filled with air. Substituting formulas (22) and (21) into (20), the total capacitance per unit length can be simplified as

$$C = \varepsilon_0 \varepsilon_{\text{eff}} \left(\frac{K(k_1)}{K(k_1')} + \frac{K(k_3)}{K(k_3')} \right) \tag{23}$$

Then the characteristic impedance of the suspended coplanar waveguide can be expressed as

$$Z = \frac{120\pi \varepsilon_{eff} \varepsilon_0}{\sqrt{\varepsilon_{eff}} C} = \frac{120\pi}{\sqrt{\varepsilon_{eff}} \left(\frac{K(k_1)}{K(k_1')} + \frac{K(k_3)}{K(k_3')} \right)} \tag{24}$$

With the help of MATLAB, the characteristic impedance of the suspended coplanar waveguide can be obtained from (24) The suspended coplanar waveguide is also simulated by HFSS, and the calculated result from (24) is compared with the simulation, as shown in Fig.5 (a) and (b). Where $a = 0.8$mm, $b = 1.1$mm, $h_1 = 0.508$mm, $h_2 = 0.254$mm, $h_3 = 1.041$mm, and $h_4 = h_3 h_2$. Z_1 is the simulated value, while Z_2 is the calculated one It is seen that the calculation and the simulation have the similar variation trend, and the error between them is within 3.1%, which verifies the reliability of the analysis and calculation process.

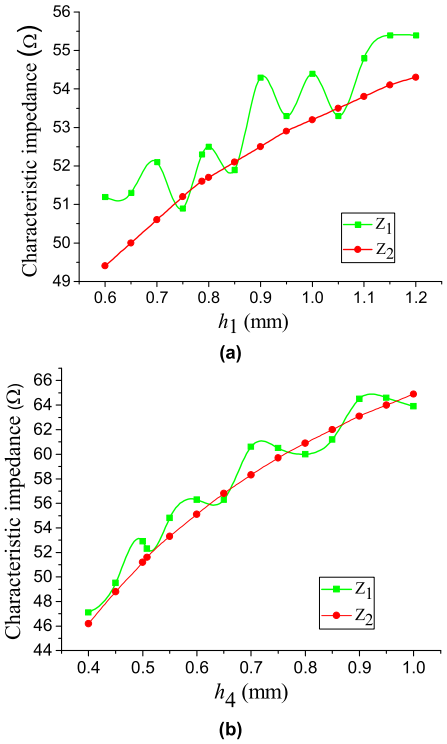

FIGURE 5. Influence of upper/lower air cavity on characteristic impedance of the suspended coplanar waveguide. (a) Characteristic impedance versus h_1, $h_4 = 0.787$mm. (b) Characteristic impedance versus h_4, $h_1 = 0.508$mm.

III. SUSPENDED COPLANAR WAVEGUIDE IMPLEMENTATION BY USING MULTI-LAYER PCB TECHNIQUE

A. A DESIGN AND ANALYSIS OF THE SELF-PACKAGED MULTI-LAYER SCPW

Based on the ideal SCPW model, a self-packaged SCPW circuit is constructed by five-substrate PCB technique, as shown in Fig.6. Where S_1 and S_5 are used for packaging, S_2 and S_4 have part PCB cut air cavities, and S_4 is used for concentrating electromagnetic field to realize the suspension, while the desired components can be set in S_2/S_4 S_3 is the main circuit Here S_i represents the i-th dielectric substrate. The PCB cut air cavity introduces reduced dielectric loss, and the two cavities have the same size of 16mm × 6mm. F_i $(i = 1, 2, \ldots, 10)$ is the upper/bottom layer of each substrate, as illustrated in Fig.6, where both F_1 and F_{10} are covered with copper for electromagnetic shielding, F_3, F_4, F_7, F_8, and F_9 are part copper covered layers, while F_5 and F_6 are the upper/bottom layers of the main circuit, respectively. The whole circuit includes grounded coplanar waveguide (GCPW or CBCPW), strip line structured GCPW, SCPW, and transition parts. Where the strip line structured GCPW is between the GCPW and the SCPW, which is a GCPW structure but imbedded in the dielectric, like that of the strip line structure. All of the circuit sections with lengths of $l_i (i = 1, 2, 3)$ have characteristic impedance of 50Ω.

In this design, the copper-covered planes are connected through the copper-covered side wall of the air cavity, as is shown in Fig.7. For the structure composed of substrate 3 and 4, it is a GCPW but make some grounded part lower to generate suspension, which is like a grounded suspended coplanar waveguide [17]. The end connections of the upper/lower air cavities and the left/right end connections of each substrate are sealed with copper for electromagnetic shielding. The rows of via holes which are perpendicular to the GCPW are used for the harmonics suppression.

Cross section of the self-packaged SCPW and its electromagnetic field is illustrated in Fig.7, where the lateral walls and the top/bottom layers have been connected to the ground, which is not only beneficial for electromagnetic shielding, but also beneficial for the circuit's mechanical strength enhancement Substrates 1 and 5 are designed using FR4, which have relative permittivity of 4.4 and thickness of 0.6mm, while substrates 2, 3, and 4 are designed using Rogers 5880 material with relative dielectric constant of 2.2, and thickness of 0.508mm, 0.254mm, and 0.787mm, respectively

The core circuit structure is shown in Fig.8, where the circuit top view and the backside view are shown in Fig.8 (a) and (b), respectively. For the certain dimensions as shown in Fig.8, the simulated circuit frequency responses versus air cavity heights of h_2 and h_4 are illustrated in Fig.9 (a) and (b), respectively. It is noted that the cavity height h_2 has important influence on the return loss, and the attenuation of S_{11} becomes poor with h_2 increasing. It also can be seen that h_4 influences both S_{11} and S_{21}, and parasitical harmonic would be produced in higher frequency band when h_4 is less than 0.508mm, which indicates that the parasitic

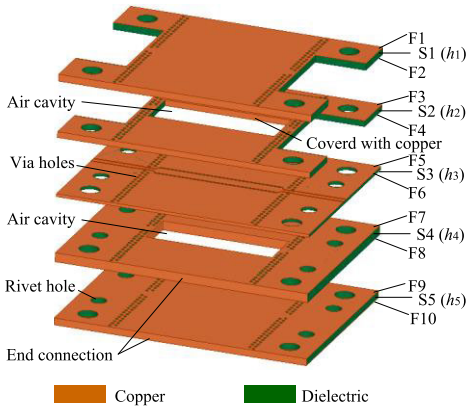

FIGURE 6. Three dimensional view of the proposed self-packaged SCPW. $S_i(i = 1, 2, 3, 4, 5)$ denotes the i-th substrate.

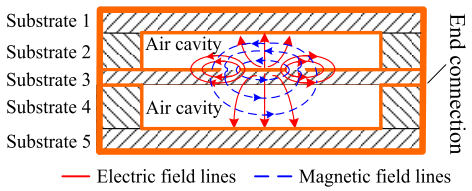

FIGURE 7. Cross section and electromagnetic field of the self-packaged SCPW.

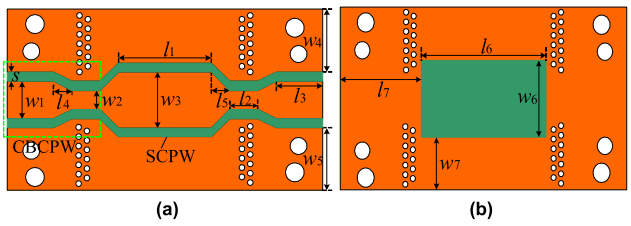

FIGURE 8. Core circuit structure. (a) Top view of the core circuit layer. (b) Backside view of the core circuit layer. $l_1 = 15.6$ $l_2 = 1.4$ $l_3 = 6.2$, $l_4 = l_5 = 0.3$, $w_1 = 0.7$, $w_2 = 0.5$ $w_3 = 1.6$, $w_4 = w_5 = 12.05$, $s = 0.2$, $l_6 = 16$, $l_7 = 8$, $w_6 = 6$, $w_7 = 9.6$. unit: mm.

modes have some relevance with the cavity height. It can be concluded from Fig.9 that 1) the air cavity height affects the transmission performance, and the transmission line has the best performance when $h_2 = 0.508$mm and $h_4 = 0.787$mm; 2) the electromagnetic wave would concentrates to the dielectric when the lower air cavity height is too small, which would increase the parasitic effects; 3) SCPW would be similar to a common CPW when the air cavity is too high, which would increase the radiation loss. Both 2) and 3) are not beneficial to the improvement of the transmission performance of the SCPW.

The proposed SCPW can be seen as a black box as shown in Fig.10, where the input/output voltage-current matrix can be formulated as

$$\begin{bmatrix} V_1 \\ I_1 \end{bmatrix} = \begin{bmatrix} A & B \\ C & D \end{bmatrix} \begin{bmatrix} V_2 \\ I_2 \end{bmatrix} \tag{25}$$

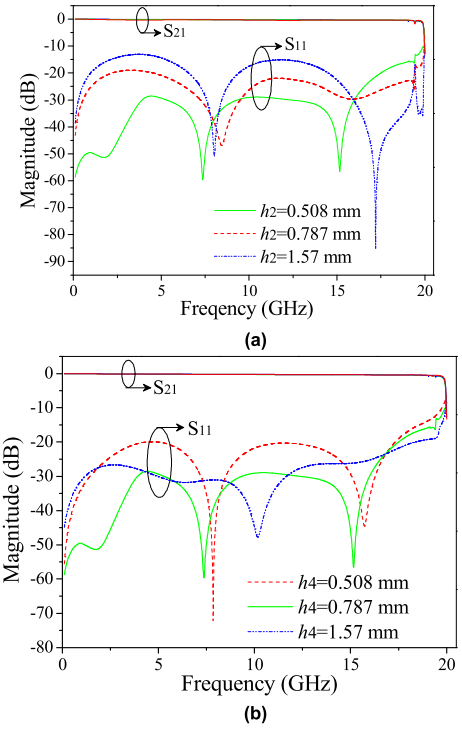

FIGURE 9. Simulated circuit frequency responses versus air cavity height. (a) Frequency responses versus h_2. (b) Frequency responses versus h_4.

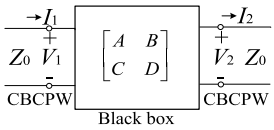

FIGURE 10. Black box of the SCPW circuit.

$$\begin{bmatrix} A & B \\ C & D \end{bmatrix} = \begin{bmatrix} A_2 & B_2 \\ C_2 & D_2 \end{bmatrix} \times \begin{bmatrix} A_1 & B_1 \\ C_1 & D_1 \end{bmatrix} \times \begin{bmatrix} A_2 & B_2 \\ C_2 & D_2 \end{bmatrix} \tag{26}$$

For the lossless case, $A_i = \cos\beta_i l_i B_i = jZ_0 \sin\beta_i l_i$, $C_i = jY_0 \sin\beta_i l_i$, $D_i = \cos\beta_i l_i$, $i = 1, 2$. $\beta_i = \omega\sqrt{\varepsilon_{re\,i}}/c$. Here, β_i is the corresponding phase constant of the SCPW transmission line, c is the velocity of light in free space, $\varepsilon_{re\,i}$ is the corresponding effective relative permittivity, and $Y_0 = 1/Z_0$, $Z_0 = 50\Omega$.

For the lossy case, the ABCD matrix of each circuit section can be formulated as [5]

$$\begin{bmatrix} A_i & B_i \\ C_i & D_i \end{bmatrix} = \begin{bmatrix} \cosh\gamma_i l_i & Z\sinh\gamma_i l_i \\ (\sinh\gamma_i l_i)/Z & \cosh\gamma_i l_i \end{bmatrix} \tag{27}$$

$$Z^2 = Z_0^2[(1+S_{11})^2 - S_{21}^2]/[(1-S_{11})^2 - S_{21}^2] \tag{28}$$

where the propagation constant γ_i can be formulated as $\gamma_i = \alpha_i + j\beta_i$, here α_i is the corresponding attenuation constant, and the ABCD matrix can be achieved as that in (27). It is noted that the ABCD matrix of the lossy circuit is complicated, and in order to simplify the computation, only the suspended section with length of l_1 is considered because the other sections such as the parts with length of l_2 have non-significant effect on the transmission line compared with

the suspended coplanar waveguide section. So, according to the relationship between the S-parameter and the ABCD matrix, the attenuation and phase constants of the SCPW can be obtained by

$$e^{-\gamma l} = e^{-(\alpha+j\beta)l} = \left\{\left[1-S_{11}^2+S_{21}^2+\sqrt{\left(S_{11}^2-S_{21}^2+1\right)^2-(2S_{11})^2}\right]/(2S_{21})\right\}^{-1} \tag{29}$$

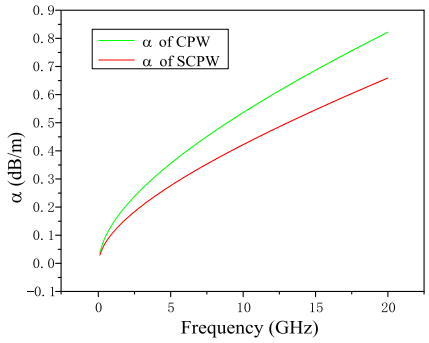

FIGURE 11. α of SCPW and of CPW versus working frequency.

Attenuation constant of the SCPW is plotted in Fig.11, where the 50Ω CPW transmission line which is used for comparison with the proposed SCPW has the same dielectric constant and thickness as that of the core circuit. It is seen from DC to 20GHz, α of the proposed SCPW is obvious smaller than that of the CPW, and α gets lower as working frequency increases.

As $c/\sqrt{\varepsilon_{re}} = \lambda_g f$ and $\beta = 2\pi/\lambda_g$, the relationship of phase constant β and frequency can be expressed as $\beta = 2\pi f\sqrt{\varepsilon_{re}}/c$, where c is the velocity of light in free space, f is the working frequency, and λ_g is the guided wavelength. It is noted that β is proportional to frequency. If the slope of $\beta - f$ curve is defined as k, the effective permittivity of the SCPW transmission line can be achieved as

$$\varepsilon_{re} = [kc/(2\pi)]^2 \tag{30}$$

Simulated electric/magnetic field distributions of the SCPW are plotted in Fig.12 (a) and (b), respectively. It shows that the electromagnetic field concentrates on the conductor strip and the gap around, especially on the suspension part, which is consistent with that shown in Fig.7

Lumped element equivalent circuit of the proposed SCPW is shown in Fig.13(a), and the simulated frequency responses comparison by electromagnetic/circuit simulators are plotted in Fig.13(b). It is seen that the circuit simulation result approaches to the electromagnetic simulation one. The circuit parameters are extracted as $C_1 = 0.1430$pF, $L_1 = 0.7374$nH, $C_2 = 0.3291$pF, $C_3 = 0.0274$pF, $L_2 = 0.7872$nH, $C_4 = 0.1595$pF

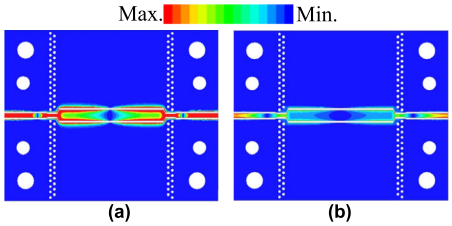

FIGURE 12. Simulated electric/magnetic field distributions. (a) Electric field distribution. (b) Magnetic field distribution.

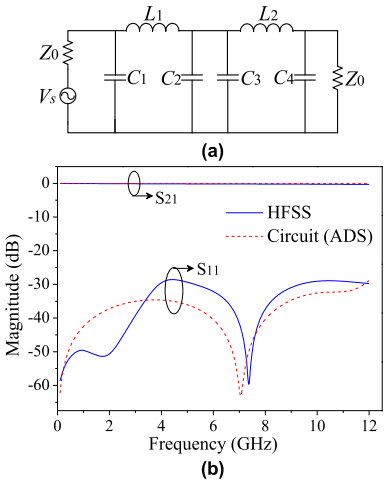

FIGURE 13. Lumped element equivalent circuit and frequency responses of the SCPW transmission line. (a) Lumped element equivalent circuit. (b) Simulated frequency responses.

B. B EXPERIMENTAL RESULTS

The proposed SCPW has been fabricated and measured, as shown in Fig.14 and Fig.15, where the fabricated individual substrate and the assembled circuit are shown in Fig.14(a) and (b) respectively, and the comparison of measurement and simulation is shown in Fig.15. The measurement is using Agilent E5071C vector network analyzer. It can be seen that the measured S_{21} agrees with the prediction, while the measured S_{11} has less attenuation compared with the simulation. The measurement and simulation difference is due to the fabrication, assembling uncertainty, and even the substrate permittivity/height tolerance. It is noted that the measured insertion loss is no more than 0.5dB from DC to 10GHz, while it is of less than 0.8dB from 10GHz to 13GHz, and the measured return loss is no less than 15.8dB from DC to 10GHz. The self-packaged SCPW has an overall circuit size of 32mm × 25.2mm × 2.75mm.

IV. APPLICATION OF THE SELF-PACKAGED SCPW IN DIPLEXER

A. BDIPLEXER DESIGN AND ANALYSIS

In order to validate the application of the presented SCPW, a high isolated and high frequency selective diplexer with mixed electric/magnetic coupling by using self-packaged suspended coplanar waveguide is designed, as shown in Fig.16.

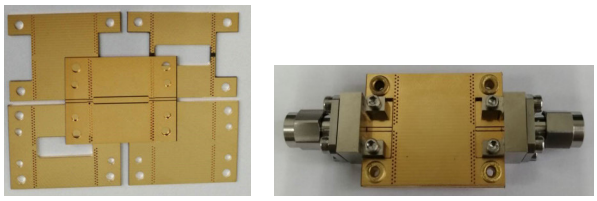

FIGURE 14. Fabricated hardware of the self-packaged multi-layer SCPW. (a) Fabricated individual substrate. (b) Assembled whole circuit.

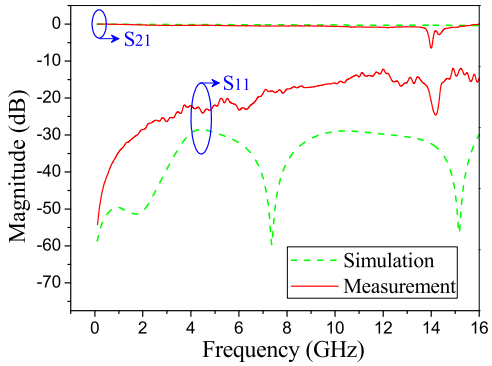

FIGURE 15. Measured S-parameter.

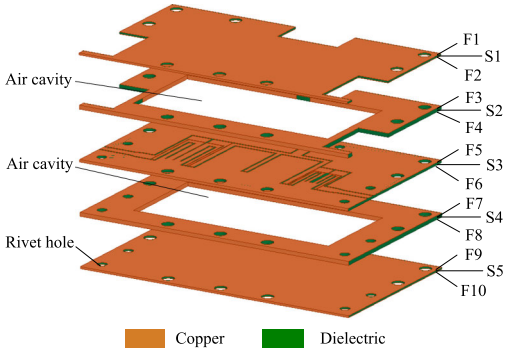

FIGURE 16. Three dimensional layered structure of the proposed self-packaged SCPW diplexer.

The diplexer is stacked with FR4 substrates for S1 and S5 with relative permittivity of 4.4 and both thickness of 0.4mm, and Rogers RT/duroid 5880 substrates for S2, S3 and S4 with relative permittivity of 2.2 and thickness of 0.508mm, 0.254mm and 0.787mm, respectively. The core circuit of the diplexer is mainly on the upper surface F5 of the core substrate S3, and part of the lower surface F6 in the position of the air cavity is etched away, so as to achieve the suspension. In order to simplify the design, the feeders of the input and output ports are designed only using the transition from SCPW to GCPW. The characteristic impedance of the input/output port is 50Ω

The core circuit (in F5) of the proposed diplexer is composed of open-circuited resonators, short-circuited resonators, and an E-shaped dual-mode resonator [18], as is shown in Fig.17. The diplexer coupling topology is plotted in Fig.18. The resonators used in the proposed diplexer

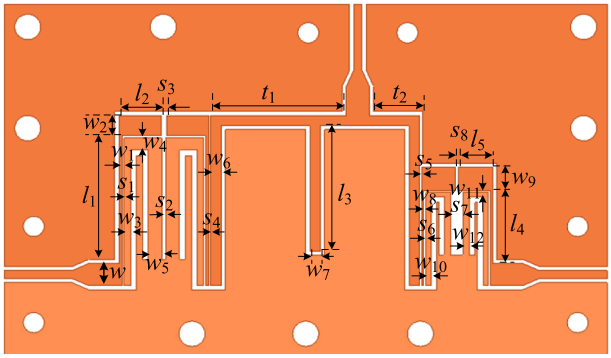

FIGURE 17. Core circuit of the SCPW diplexer.

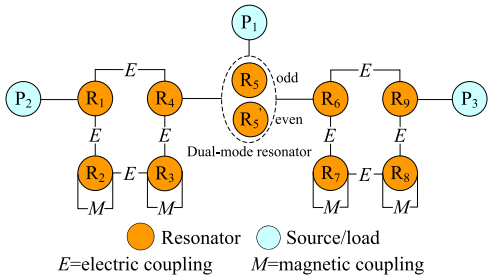

FIGURE 18. Multi-resonator coupling topology of the proposed diplexer.

are shown in Fig.19(a), (b) (c), (d) and (e), respectively. Where, the open-circuited resonators are denoted by R1/R4/R6/R9, while the short-circuited resonators are denoted by R2/R3/R7/R8, and the odd/even-mode of the E-shaped resonator are denoted by R5 and R5', respectively. The odd/even-mode of the E-shaped resonator works at different resonant frequency, which can be designed corresponding to the working frequency of the lower/upper channel of the diplexer. Set $\theta_a = \theta_{a1} + \theta_{a2}$ the input admittance of the odd/even-mode of the E-shaped resonator can be formulated respectively as

$$Y_{in,od} = -j\frac{1}{Z_a \tan\theta_a}, \quad Y_{in,e\,v} = j\frac{Z_a \tan\theta_b + Z_b \tan\theta_a}{Z_a\,(Z_b - \tan\theta_a \tan\theta_b)} \tag{31}$$

The diplexer design scheme is that the coupling of R1-R2-R3-R4 with the odd-mode of the E-shaped resonator generates the diplexer lower frequency channel, while the coupling of R6-R7-R8-R9 with the even-mode of the E-shaped resonator generates the diplexer higher frequency channel, and all of the coupling constitutes mixed electromagnetic coupling. Multiple transmission zeros can be produced by multiple resonators coupling through multiple electromagnetic paths In order to achieve high isolation of the two channel filters, the right out-of-band transmission zero of the lower frequency filter is designed near the center frequency of the higher frequency filter, while the left out-of-band transmission zero of the higher frequency filter is designed near the center frequency of the lower frequency filter.

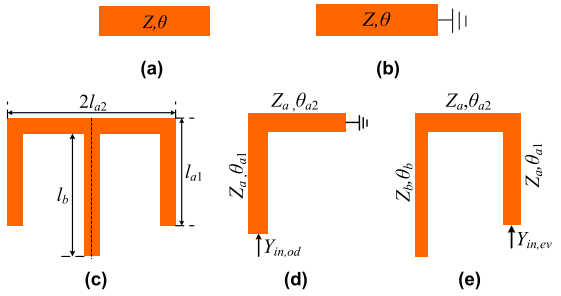

FIGURE 19. Resonators used in the proposed diplexer. (a) Open-circuited resonator. (b) Short-circuited resonator. (c) E-shaped resonator. (d) Odd-mode circuit of the E-shaped resonator. (e) Even-mode circuit of the E-shaped resonator.

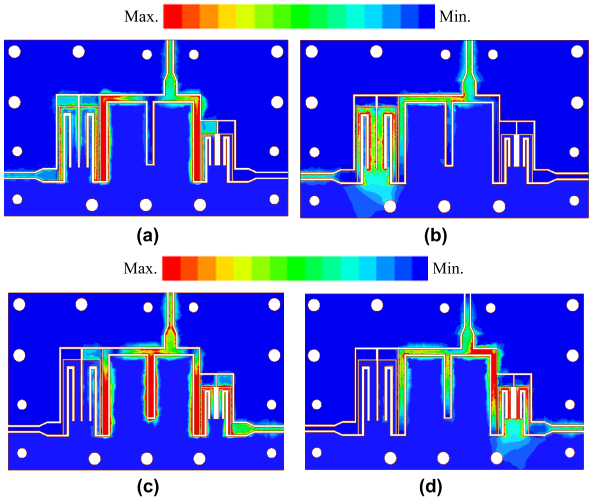

FIGURE 20. Simulated electromagnetic field distributions of the SCPW diplexer. (a) Electric field distribution at 2.53GHz. (b) Magnetic field distribution at 2.53GHz. (c) Electric field distribution at 3.75GHz. (d) Magnetic field distribution at 3.75GHz.

When the diplexer is designed working at 2.53/3.75GHz with fractional bandwidth of 9.6%/6.0%, return loss of more than 20dB, and isolation of no less than40dB, the coupling matrices of the two channels including the source and load can be formulated as (32) and (33), shown at the bottom of the page.

The actual coupling coefficient can be obtained as $k_{ij} = k_{ji} = M_{ij} \times \text{FBW}$. The diplexer physical dimensions can be calculated by the diplexer specifications, the resonant conditions ($Y_{in} = 0$) of open and short-circuited resonators, the E-shaped dual-mode resonator, and the coupling coefficients, and the circuit size can be obtained as $w = 2.2$, $w_1 = 0.4$, $l_1 = 12.8$, $w_2 = 2$, $l_2 = 8.6$, $w_3 = 0.6$, $w_4 = 1.2$, $w_5 = 1.3$, $s_1 = 0.2$, $s_2 = 0.4$, $s_3 = 0.5$, $s_4 = 0.2$, $w_6 = 1$, $t_1 = 13$, $t_2 = 4.8$, $w_7 = 1$, $l_3 = 12.4$, $s_5 = 0.2$, $s_6 = 0.2$, $s_7 = 1.2$, $s_8 = 0.3$, $w_8 = 0.2$, $l_4 = 7.1$, $w_9 = 2.3$, $l_5 = 6.8$, $w_{10} = 0.5$, $w_{11} = 0.4$, and $w_{12} = 0.6$, unit: mm

Simulated electromagnetic field distributions of the SCPW diplexer at 2.53/3.75GHz are shown in Fig.20. It is seen that when working at 2.53GHz, the electromagnetic field of the diplexer concentrates on R1-R2-R3-R4 and the odd-mode part of E-shaped resonator, as shown in Fig.20(a) and (b), while when working at 3.75GHz, the diplexer electromagnetic field concentrates on R6-R7-R8-R9 and the even-mode part of the E-shaped resonator, as shown in Fig.20(c) and (d). Electric field is dominantly concentrates on open-circuited resonator such as R1/R4/R6/R9 and the coupling gap, while the magnetic field is dominantly concentrates on short-circuited resonator such as R2/R3/R7/R8. All these are accordance with the diplexer design scheme and the coupling topology shown in Fig.18.

Multiple transmission zeros (TZs) have been introduced by the multi-resonator coupling topology, as shown in Fig.21. Transmission zeros can be controlled/adjusted by electric/magnetic coupling, for example, for the lower frequency channel, TZ1 and TZ3 can be controlled/adjusted by the resonator coupling gap (electric coupling) S_3, as shown

$$\boldsymbol{M}1 = \begin{array}{c} \\ \text{S} \\ \text{R1} \\ \text{R2} \\ \text{R3} \\ \text{R4} \\ \text{R5} \\ \text{L} \end{array} \begin{array}{c} \begin{array}{ccccccc} \text{S} & \text{R1} & \text{R2} & \text{R3} & \text{R4} & \text{R5} & \text{L} \end{array} \\ \begin{bmatrix} 0 & 1.796 & 0 & 0 & 0 & 0 & 0 \\ 1.796 & -0.486 & 2.037 & 0.272 & -0.027 & 0 & 0 \\ 0 & 2.037 & -0.773 & 1.189 & 0 & 0 & 0 \\ 0 & 0.272 & 1.189 & -0.384 & 1.194 & 0 & 0 \\ 0 & -0.027 & 0 & 1.194 & 0.458 & 2.055 & 0 \\ 0 & 0 & 0 & 0 & 2.055 & 0.486 & 1.796 \\ 0 & 0 & 0 & 0 & 0 & 1.796 & 0 \end{bmatrix} \end{array} \tag{32}$$

$$\boldsymbol{M}2 = \begin{array}{c} \\ \text{S} \\ \text{R9} \\ \text{R8} \\ \text{R7} \\ \text{R6} \\ \text{R5}' \\ \text{L} \end{array} \begin{array}{c} \begin{array}{ccccccc} \text{S} & \text{R9} & \text{R8} & \text{R7} & \text{R6} & \text{R5'} & \text{L} \end{array} \\ \begin{bmatrix} 0 & 1.976 & 0 & 0 & 0 & 0 & 0 \\ 1.976 & 0.667 & 2.419 & 0.432 & 0.035 & 0 & 0 \\ 0 & 2.419 & 1.113 & 1.383 & 0 & 0 & 0 \\ 0 & 0.432 & 1.383 & 0.499 & 1.405 & 0 & 0 \\ 0 & 0.036 & 0 & 1.405 & 0.622 & 2.457 & 0 \\ 0 & 0 & 0 & 0 & 2.457 & 0.667 & 1.976 \\ 0 & 0 & 0 & 0 & 0 & 1.976 & 0 \end{bmatrix} \end{array} \tag{33}$$

in Fig.21(a), while for the higher frequency channel, TZ5 can be controlled/adjusted by the resonator coupling gap S_8, as shown in Fig.21(b). It can be seen that TZ1/TZ3/TZ5 will be further away from center frequency with coupling gap increasing, while TZ2/TZ4 nearly stays fixed. TZ1/TZ5 also can be adjusted by S_2/S_7, respectively.

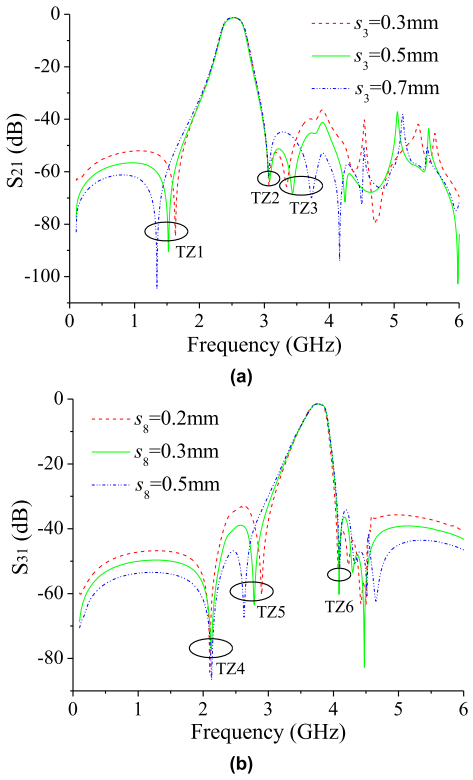

FIGURE 21. Influence of coupling gap on transmission zeros. (a) TZ versus S_3. (b) TZ versus S_8.

Influence of l_3 on diplexer bandwidth of the higher frequency channel is shown in Fig.22. It is seen that higher frequency channel bandwidth decreases with the even-mode circuit size of the E-shaped resonator increasing, so the circuit bandwidth can be adjusted. The lower frequency channel bandwidth also can be adjusted by the odd-mode circuit of the E-shaped resonator. The changing of diplexer bandwidth is due to the changing of electromagnetic coupling introduced by the changing of circuit dimension.

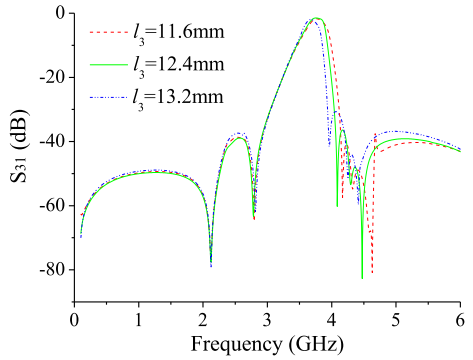

FIGURE 22. Influence of l_3 on diplexer bandwidth.

The proposed self-packaged SCPW diplexer is fabricated and measured, as shown in Fig.23 and Fig.24, respectively. The fabricated individual substrate and the assembled whole circuit are plotted in Fig.23(a) and (b), respectively, while the measured S_{11}/S_{21}/S_{31} and isolation which have been carried out by Agilent E5071C vector network analyzer are demonstrated in Fig.24(a) and (b), respectively It is seen that the presented diplexer has measured insertion loss of 1.05dB and 1.1dB respectively for the lower and higher frequency channel, and the diplexer out-of-band suppression is more than 37dB, while the measured isolation is no less than 42.5dB. Measurement is similar to the prediction, and the discrepancy between experimental results and prediction is due to the fabrication uncertainty and system error caused

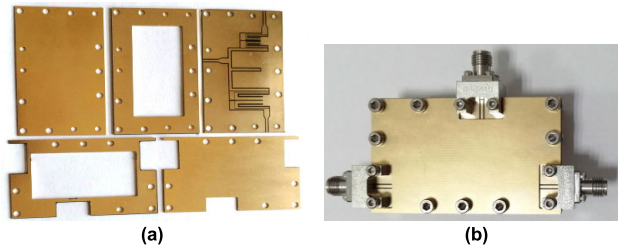

FIGURE 23. Fabricated hardware. (a) Fabricated individual substrate. (b) Assembled whole circuit.

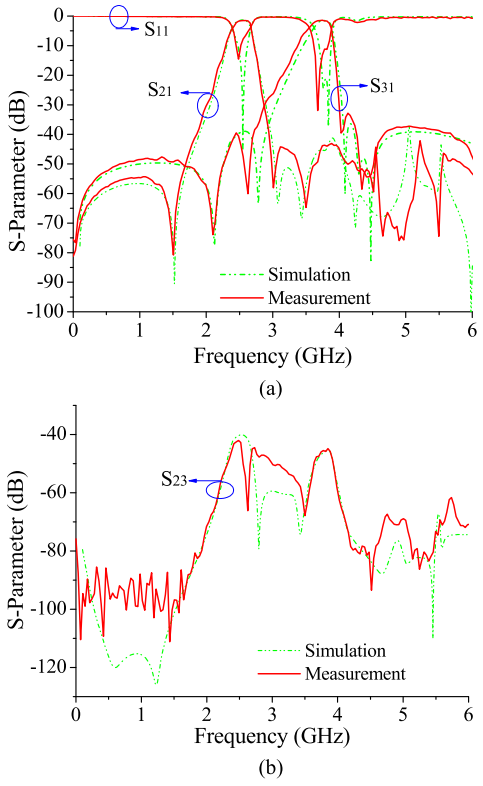

FIGURE 24. Experimental results. (a) Measured diplexer S_{11}/S_{21}/S_{31}. (b) Measured diplexer isolation.

by the vector network analyzer. The diplexer circuit size is 20.6mm × 41.6mm, which is about $0.25\lambda_g \times 0.51\lambda_g$, where λ_g is the guided wavelength at the lower frequency channel.

Comparison of this work with the related reports is shown in Table 2. It is seen that less passband insertion loss, better out-of-band suppression, more transmission zeros, and even smaller ciecuit size have been realized compared with the related reports.

TABLE 2. Comparison of this work with the related reports.

Ref.	CF (GHz)	IL (dB)	Iso. (dB)	TZs	CT	SP	CS (λ_g^2)
[19]	1.5/1.76	2.8/3.2	>30	7	M	no	0.34×0.54
[20]	1.1/1.3	1.8/1.5	>26	1	M	no	0.82×0.86
[21]	1.95/2.14	1.2/1.5	>35	3	M	no	0.36×0.38
[22]	5/5.25	1.8/1.5	>40	6	SIW	no	1.02×2.08
[23]	0.8/2.5	1.26/1.21	>45	7	SISL	yes	-
ours	2.53/3.75	1.05/1.1	>42.5	8	SCPW	yes	0.25×0.51

Ref.: reference, CF: center frequency, IL: insertion loss, Iso.-isolation, CT: Circuit type, M: microstrip, SP: self-packaging CS: circuit size.

V. APPLICATION OF THE SELF-PACKAGED SCPW IN REFLECTIONLESS BANDSTOP FILTER

A simple reflectionless bandstop filter (RBSF) with absorptive resistors is also designed, as is shown in Fig.25. Here S_1 and S_5 are designed using FR4 substrate with relative permittivity of 4.4, and thickness of 0.6mm, both S_2 and S_4 have relative permittivity of 2.2, and thickness of 1.57mm, while S_3 is with Rogers 3010 which has a relative dielectric constant of 10.2, and thickness of 0.635mm. The main circuit is composed of two pairs of asymmetric U-shaped slots in the ground and a pair of absorptive resistors bounded to the first stage defection, as is plotted in Fig.26(a), and the lumped element equivalent circuit is plotted in Fig.26(b). The resistors are used to absorb the reflection signal, and matching in a certain frequency band can be obtained.

The SCPW RBSF is designed with a center frequency of 1.84GHz, a 3dB fractional bandwidth (FBW) of 24.7%, and a return loss of no less than 15dB. ε_{re} of the suspended circuit can be obtained as 6.4044, while the guided wavelength at 1.84GHz can be achieved by $\lambda_g = c/(\sqrt{\varepsilon_{re}}f)$ as 64.44mm. As a microwave filter is usually implemented by a quarter-wavelength resonator, and according to the filter specifications, the circuit dimensions can be obtained as $w = 0.54$,

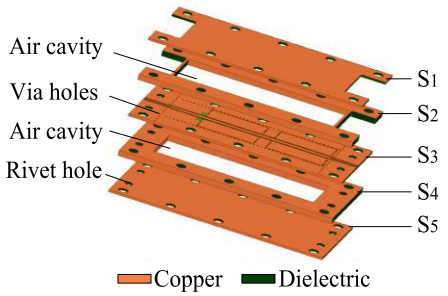

FIGURE 25. Self-packaged SCPW RBSF.

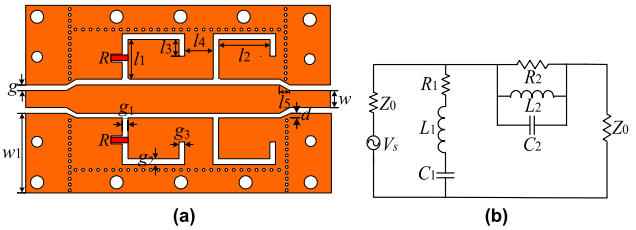

FIGURE 26. Core circuit structure and lumped element equivalent circuit of the SCPW RBSF. (a) Structure of the core circuit. (b) Lumped element equivalent circuit of the RBSF.

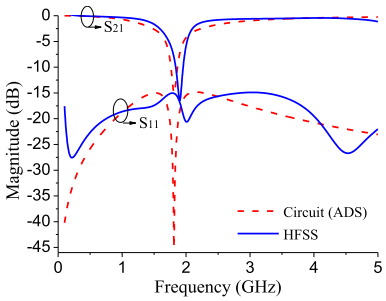

FIGURE 27. Circuit/EM simulated S-parameter of the proposed SCPW RBSF.

$g = 0.5, l_1 = 5, l_2 = 15, l_3 = 4.5, l_4 = 3, l_5 = 0.7, g_1 = g_2 = g_3 = 0.2$, unit: mm. $R = 120\Omega$. Here l_2 which approaches to $\lambda_g/4$ (16.11mm) is dominantly used for controlling the filter center frequency.

For the lumped element equivalent circuit of the proposed RBSF shown in Fig.26(b), the simulated S-parameter of the lumped element equivalent circuit by using ADS and the electromagnetic simulation result by HFSS is shown in Fig.27. Where the extracted circuit parameters are $R_1 = 60\Omega$, $L_1 = 8.5$nH, $C_1 = 0.9$pF, $L_2 = 0.7$nH, $C_2 = 11$pF, $R_2 = 232\Omega$. R_1 is equivalent to two parallel patch resistors with a value of 120Ω. It can be seen from the S-parameter comparison that the circuit simulation result approaches to the electromagnetic simulation one.

Simulated filter frequency responses variation versus l_1, l_2, g_2 and R are shown in Fig.28 (a), (b), (c) and (d), respectively. It is seen that 1) vertical length of the asymmetric U-shaped slot l_1 has weak influence on filter S_{11} and S_{21}, as shown in Fig.28 (a), but it is different for the horizontal slot length l_2, and the circuit working frequency increases with l_2 decreasing. It is noted that S_{11} has an attenuation of more than 13dB within 5GHz in the cases shown in Fig.28(a), (b) and (c), and the maximum attenuation is more than 35dB, as shown in Fig.28 (b); 2) horizontal slot width g_2 has slight effect on S_{11}/S_{21}, and parasitic harmonic will be introduced with g_2 increasing, as shown in Fig.28(c); 3) The loading resistors are very important for RBSF. It is noted that when $R = 50\Omega$, S_{11} attenuation is less than 10dB, and when $R = 120\Omega$, the attenuation is about 15dB, while when $R = 10000\Omega$, the reflectionless phenomenon disappears because this case

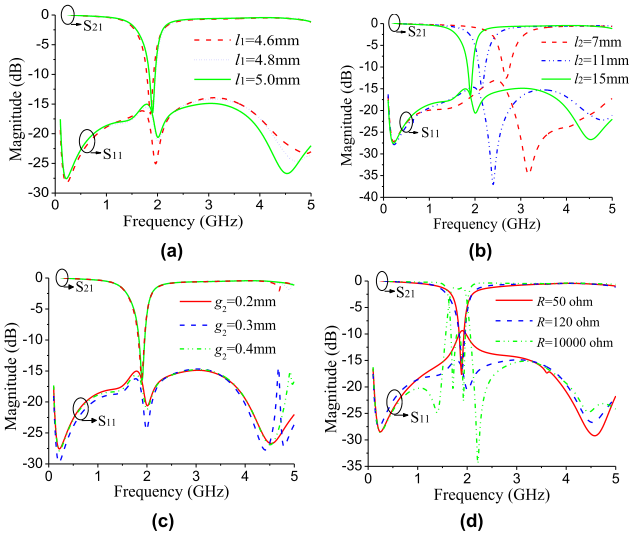

FIGURE 28. Simulated frequency responses variation versus some physical parameters and R. (a) Variation of frequency responses with l_1. (b) Variation of frequency responses with l_2. (c) Variation of frequency responses with g_2. (d) Variation of frequency responses with resistor R.

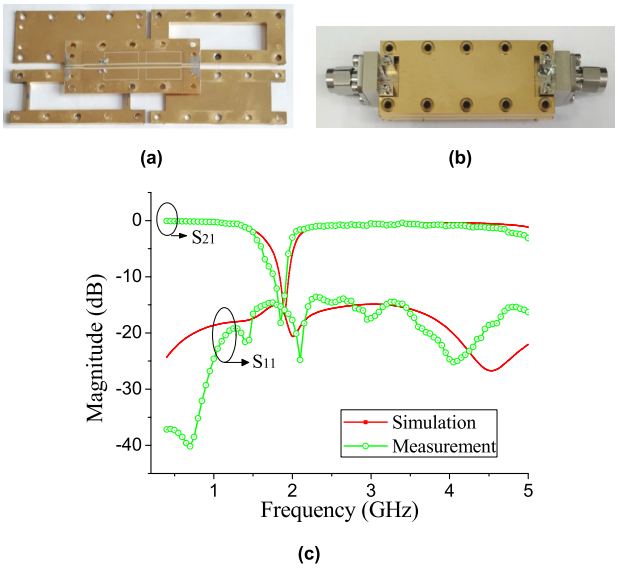

FIGURE 29. Fabrication and measured results of the self-packaged SCPW RBSF. (a) Fabricated individual substrates. (b) Whole circuit hardware. (c) Measured results.

is similar to an open circuited one and a favorable reflective bandstop filter is obtained, as Fig.28(d) demonstrates.

The multi-layer SCPW RBSF has been fabricated and tested, as illustrated in Fig.29(a) (b)and (c), respectively. It can be seen that the proposed SCPW RBSF has a measured working frequency of 1.76GHz, a measured bandwidth of about 27.3%, and a measured S_{11} attenuation of no less than 13.8dB from DC to 5GHz. The measurement approaches to the simulation, and the discrepancy between measurement and prediction is due to the material tolerance and fabrication uncertainty. The proposed SCPW RBSF has a size of $0.21\lambda_g \times 0.67\lambda_g$ (43.4mm $\times$ 13.8mm), where λ_g is the guided wavelength at 1.84GHz.

TABLE 3. Comparison of this work with the related reports.

Ref.	CT	CF (GHz)	FBW (%)	S_{11}	SP	Size (λg^2)
[24]	M	2	8	>10dB, DC-6GHz	no	-
[25]	M	2.33	12	>10dB, 1.5-3.5GHz	no	-
[26]	M	2	86.5	>12.2dB, 0-4GHz	no	0.18
[27]	M	2	1	>10dB, 0-8GHz	no	-
ours	SCPW	1.76	27.3	>13.8dB, DC-5GHz	yes	0.141

Comparison of the proposed reflectionless bandstop filter and the related works is listed in Table 3. It is seen that the presented self-packaged SCPW RBSF not only has more S_{11} attenuation, and even wider bandwidth, but also has smaller circuit size compared with some related reports. The availability of the proposed SCPW has been demonstrated.

VI. CONCLUSION

Suspended coplanar waveguide model is analyzed by using conformal mapping method, and a multi-layer self-packaged SCPW transmission line with wideband and low insertion loss has been proposed and manufactured by using common PCB technique. The attenuation constant of the SCPW has been extracted, and a smaller attenuation constant compared to the traditional CPW has been demonstrated. Based on the self-packaged SCPW transmission line, a multi-resonator coupled diplexer with high frequency selectivity and high isolation has been implemented. Diplexer isolation and out-of-band suppression have been effectively improved by assigning the transmission zeros of each channel filter to the passband of the other channel filter, and the transmission zeros can be controlled/adjusted by electric/magnetic couplings. A reflectionless bandstop filter is also developed for demonstrating the availability of the proposed self-packaged SCPW. The advantages of wideband and low loss of the self-packaged SCPW, and high frequency selectivity as well as high isolation of the proposed SCPW diplexer, and matching of the proposed SCPW RBSF have been demonstrated. All of the proposed SCPW circuits have been fabricated and demonstrated by experiment.

The proposed SCPW circuits have advantages of self-packaging, low loss because of the low electromagnetic leakage, and desired components including power source, integrated circuit chips and dielectric resonators, et al can be placed in the reserved air cavities, and simultaneously, more vertical integration can also be implemented.

REFERENCES

[1] W. Schwab, F. Begelsack, and W. Menzel, "Multilayer suspended stripline and coplanar line filters," *IEEE Trans. Microw. Theory Techn.*, vol. 42, pp. 1403–1407, Jul. 1994.

[2] W. Menzel and D. Talabur, "Quasi-lumped suspended stripline bandstop filters," *Electron. Lett.*, vol. 45, no. 17, pp. 897–898, Aug. 2009.
[3] R. Ruf and W. Menzel, "A novel compact suspended stripline resonator," *IEEE Microw. Wireless Compon. Lett.*, vol. 22, no. 9, pp. 444–446, Sep. 2012.
[4] I.-H. Kang, Y.-G. Kim, D.-S. Woo, S.-K. Kim, and K. W. Kim, "Design of a tunable oscillator using a suspended-stripline resonator," in *Proc. 7th Eur. Microw. Conf. (EuMIC)*, Amsterdam, The Netherlands, Oct. 2012, pp. 762–765.
[5] L. G. Maloratsky, "Reviewing the basics of suspended striplines," *Microw. RF*, vol. 45, no. 10, pp. 82–98, 2002.
[6] Y. Wu, K.-S. Chin, W. Che, K.-C. Chang, and W. Feng, "LTCC multilayered helical filters with a mixed electric and magnetic coupling structure," *IEEE Trans. Compon., Packag., Manuf. Technol.*, vol. 5, no. 8, pp. 1050–1059, Aug. 2015.
[7] K. Ma and K. T. Chan, "Quasi-planar circuits with air cavities," PCT WO Patent 2007 149 046, Dec. 27, 2007.
[8] A. Sieganschin, T. Jaschke, H. K. Mitto, N. J. Lamann, J. Waldhelm, and A. F. Jacob, "A compact low-loss multilayer SIW diplexer at K/Ka-band," in *Proc. 12th German Microw. Conf. (GeMiC)*, Stuttgart, Germany, Mar. 2019, pp. 51–54.
[9] K. C. Gupta, R. Garg, and I. J. Bahl, *Microstrip Lines and Slotlines*. Norwood, MA, USA: Artech House, 1979.
[10] C. P. Wen, "Coplanar waveguide: A surface strip transmission line suitable for nonreciprocal gyromagnetic device applications," *IEEE Trans. Microw. Theory Techn.*, vol. MTT-17, no. 12, pp. 1087–1090, Dec. 1969.
[11] R. W. Jackson, "Considerations in the use of coplanar waveguide for millimeter-wave integrated circuits," *IEEE Trans. Microw. Theory Techn.*, vol. MTT-34, no. 12, pp. 1450–1456, Dec. 1986.
[12] G. Ghione and C. U. Naldi, "Coplanar waveguides for MMIC applications: Effect of upper shielding, conductor backing, finite-extent ground planes, and line-to-line coupling," *IEEE Trans. Microw. Theory Techn.*, vol. MTT-35, no. 3, pp. 260–267, Mar. 1987.
[13] G. Ghione and C. Naldi, "Analytical formulas for coplanar lines in hybrid and monolithic MICs," *Electron. Lett.*, vol. 20, no. 4, p. 179, 1984.
[14] E. Chen and S. Y. Chou, "Characteristics of coplanar transmission lines on multilayer substrates: Modeling and experiments," *IEEE Trans. Microw. Theory Techn.*, vol. 45, no. 6, pp. 939–945, Jun. 1997.
[15] M. Y. Frankel, R. H. Voelker, and J. N. Hilfiker, "Coplanar transmission lines on thin substrates for high-speed low-loss propagation," *IEEE Trans. Microw. Theory Techn.*, vol. 42, no. 3, pp. 396–402, Mar. 1994.
[16] S.-J. Fang, "Study on the properties of asymmetric coplanar waveguides and their field structure diagrams," Ph.D. dissertation, Dept. Electron. Eng., Dalian Maritime Univ., Dalian, China, 2001.
[17] J. Xiao and L. Yang, "Self-packaged grounded suspended coplanar waveguide structure," *Electron. Lett.*, vol. 55, no. 15, pp. 841–843, Jul. 2019.
[18] J. Xiao, M. Zhang, and J. Ma, "A compact and high-isolated multiresonator-coupled diplexer," *IEEE Microw. Wireless Compon. Lett.*, vol. 28, no. 11, pp. 999–1001, Nov. 2018.
[19] C.-F. Chen, T.-Y. Huang, C.-P. Chou, and R.-B. Wu, "Microstrip diplexers design with common resonator sections for compact size, but high isolation," *IEEE Trans. Microw. Theory Techn.*, vol. 54, no. 5, pp. 1945–1952, May 2006.
[20] D. Chen, L. Zhu, H. Bu, and C. Cheng, "A novel planar diplexer using slotline-loaded microstrip ring resonator," *IEEE Microw. Wireless Compon. Lett.*, vol. 25, no. 11, pp. 706–708, Nov. 2015.
[21] X. Guan, F. Yang, H. Liu, and L. Zhu, "Compact and high-isolation diplexer using dual-mode stub-loaded resonators," *IEEE Microw. Wireless Compon. Lett.*, vol. 24, no. 6, pp. 385–387, Jun. 2014.
[22] K. Song, Y. Zhou, Y. Chen, A. M. Iman, S. R. Patience, and Y. Fan, "High-isolation diplexer with high frequency selectivity using substrate integrate waveguide dual-mode resonator," *IEEE Access*, vol. 7, pp. 116676–116683, 2019.
[23] Y. Chu, K. Ma, and Y. Wang, "A high isolation and low loss duplexer based on SISL platform," in *IEEE MTT-S Int. Microw. Symp. Dig.*, Philadelphia, PA, USA, Jun. 2018, pp. 525–528.
[24] J. Lee and J. Lee, "Distributed-element reflectionless bandstop filter with a broadband impedance matching," *IEEE Microw. Wireless Compon. Lett.*, vol. 30, no. 6, pp. 561–564, Jun. 2020.
[25] R. Gómez-García, J.-M. Muñoz-Ferreras, and D. Psychogiou, "Symmetrical quasi-reflectionless BSFs," *IEEE Microw. Wireless Compon. Lett.*, vol. 28, no. 4, pp. 302–304, Apr. 2018.
[26] M. Kong, Y. Wu, Z. Zhuang, Y. Liu, and A. A. Kishk, "Compact wideband reflective/absorptive bandstop filter with multitransmission zeros," *IEEE Trans. Microw. Theory Techn.*, vol. 67, no. 2, pp. 482–493, Feb. 2019.
[27] J. Lee and J. Lee, "Arbitrary-order distributed-element narrowband reflectionless bandstop filter with canonical transmission response and broadband matching," *IEEE Trans. Microw. Theory Techn.*, vol. 68, no. 10, pp. 4381–4389, Oct. 2020.

JIAN-KANG XIAO (Member, IEEE) received the B.S. degree in electronics and the M.S. degree in radio physics from Lanzhou University, China, in 1996 and 2004, respectively, and the Ph.D. degree from Shanghai University, China, in 2007. Then, he joined the South China University of Technology, China, as a Postdoctoral Research Fellow, from 2007 to 2009. He worked at Hohai University, China, from April 2009 to June 2011, where he was awarded as one of the first batch of Changzhou city's "831 High-level Innovation and Entrepreneurship Talent Project," in 2009. He joined Xidian University, China, in July, 2011. He was an Academic Visitor with Tianjin University, China, and Heriot-Watt University, U.K., from 2013 to 2014 and from 2015 to 2016, respectively. He has authored a special subject in *Wiley Encyclopedia of Electrical and Electronics Engineering* and a monograph on planar circuits. He has also authored/coauthored more than 100 international journal articles and conference reports, and was a reviewer for about ten IEEE TRANSACTIONS, IEEE and IET journals. His research interests include microwave passive components, antennas, and wireless technologies.

JIAO ZHANG was born in Gansu, China. She received the B.S. degree in measurement and control technology and instrumentation from Lanzhou Jiaotong University, China, in 2018. She is currently pursuing the M.S. degree with Xidian University, China. Her research interest includes self-packaged suspended coplanar waveguide microwave filter/diplexer design.

JUN PU was born in Henan, China. He received the B.S. and M.S. degrees in measurement and control technology and instrumentation from Xidian University, China, in 2017 and 2020, respectively His research interest includes microwave self-packaged suspended coplanar waveguide filter design.